

ARTICLES

**Absolute measurement of the differential cross section
for the reaction ${}^4\text{He}(\gamma, p){}^3\text{H}$ from 63 to 71 MeV**

R. T. Jones* and D. A. Jenkins

*Physics Department, Virginia Polytechnic Institute and State University, Blacksburg, Virginia 24061*P. T. Debevec, P. D. Harty,[†] and J. E. Knott*Nuclear Physics Laboratory and Department of Physics, University of Illinois at Urbana-Champaign,
Champaign, Illinois 61820*

(Received 26 December 1990)

Results are presented from a ${}^4\text{He}$ photodisintegration experiment performed with quasi-monochromatic photons using a large solid-angle detector. The tagged-bremsstrahlung technique gave a reliable absolute normalization. In addition, an unambiguous separation of the proton-triton channel from other photodisintegration channels was achieved. A total cross section of $218 \pm 8 \mu\text{b}$ was measured at a mean energy of 67 ± 4 MeV and Legendre coefficients up to a_5 were extracted from the angular distributions.

I. INTRODUCTION

The photodisintegration of ${}^4\text{He}$ below pion threshold has been the subject of several theoretical and experimental investigations. Since ${}^4\text{He}$ has a particularly simple closed-shell configuration in its ground state, and the electromagnetic interaction is well known, the general features of the photodisintegration cross section are simple to interpret within the framework of the nuclear shell model. Nevertheless, there are marked deviations from such a simple model, which contain new information about the nuclear current in the ground state and the reaction mechanism.

Most of the work to date has concentrated on the two-body photodisintegration channels, due to the complexity of a three or four-body final state. There are three two-body channels: ${}^4\text{He}(\gamma, p){}^3\text{H}$, ${}^4\text{He}(\gamma, n){}^3\text{He}$, and ${}^4\text{He}(\gamma, {}^2\text{H}){}^2\text{H}$. The symmetric deuteron channel opens up at 23.9 MeV, but being $E1$ forbidden, the cross section is a fraction of a percent of the other two.

An early calculation of the total cross section, by Londergan and Shakin, used shell-model wave functions both for the initial ground state and the final continuum state.¹ Further refinements within this framework were made by others.²⁻⁴ These calculations showed a peak in the total cross section just above threshold, due to the $E1$ resonance, with a monotonically decreasing tail extending up to the limits of the calculation between 50 and 100 MeV.

A comprehensive study of ${}^4\text{He}$ photodisintegration within the shell model was published by Gari and Hebach,⁵ in which they decomposed the total cross sec-

tion into components arising from the shell-model nucleonic current, the mesonic current (using Siegert's theorem⁶), and nucleon correlations which they added as a correction to the independent-particle shell-model states. They showed that the cross section above 50 MeV actually has very little contribution from the nucleonic current, and is dominated by meson-exchange effects.

There have also been some recent results from groups applying "exact" techniques to the solution of scattering in few-nucleon systems. Although a full calculation including three- and four-particle continuum states has not yet appeared, there are limited regions where the calculations are simplified and cross sections for two-body channels have been presented.^{7,8} One of these regions is just above the two-body threshold, before the three-body and four-body channels have opened up, and another is in the region above 50 MeV and below the pion production threshold, where final-state interactions are suppressed. Experimental results are presented in this paper for the ${}^4\text{He}(\gamma, p){}^3\text{H}$ reaction in the region between 63 and 71 MeV.⁹

The first ${}^4\text{He}(\gamma, p){}^3\text{H}$ measurements were performed using the inverse reaction ${}^3\text{He}(p, \gamma){}^4\text{He}$ with the assumption of detailed balance.^{10,11} The measurements spanned the range 3–20 MeV proton energy, which corresponds to 23–40 MeV photon energy, the region of the giant dipole resonance (GDR). These measurements concentrated on the GDR region, and only a few results exist for the energy region between 50 MeV and the pion threshold.

The single most comprehensive data set, spanning the energy region from threshold to 260 MeV, was performed with a bremsstrahlung photon beam and a cloud

chamber.¹² The energy of the photon was determined from the tracks of the charged particles. Both total cross sections and angular distributions were measured. Due to the inherent statistics limitations of cloud-chamber experiments, the data had to be binned on a very coarse grid. A single angular distribution was used for the energy range from 65 to 170 MeV. Another group using similar techniques has also reported results for this reaction.¹³⁻¹⁵ Other measurements have been reported of the total cross section.^{16,17} The experiments indicate that at 70 MeV the (γ, p) and (γ, n) cross sections are each about 35% of the total cross section, the three-body channel (γ, pnd) is about 25% of the total cross section, the four-body channel $(\gamma, ppnn)$ is about 5% of the total cross section, and the (γ, dd) channel is less than 1% of the total cross section of 650 μb .

Many of the early experiments used bremsstrahlung; however, this beam contains a continuum of photon energies whereas the normalization for an absolute cross section requires a determination of the flux of photons within a certain narrow energy interval. This normalization is simplified by the use of "photon tagging," in which the post-bremsstrahlung electrons are analyzed in a magnetic spectrometer and detected in coincidence with reaction products. The incident electron beam energy minus the recoil electron energy gives the energy of the bremsstrahlung photon, and counting the recoil electrons as a function of energy provides an accurate absolute normalization. The measurement reported in this paper was performed at the University of Illinois Nuclear Physics Laboratory tagged-photon facility, using a large acceptance detector constructed for photodisintegration experiments on light nuclei.

II. EXPERIMENTAL SETUP

A. Monochromator

The photon beam was produced by the method of bremsstrahlung tagging. In this method an electron of known energy radiates a photon in a thin foil. The post-bremsstrahlung electron is momentum analyzed and detected in the focal plane of a magnetic spectrometer. The energy of the photon is given by the difference between the initial and final electron energies. The measurement of the time difference between the detection of an electron in the tagger focal plane and a reaction product in the detector correlates each event with a photon energy.

Electrons from the 100% duty factor accelerator MUSL-2 were focused to a spot of about 2 mm in diameter on a 127- μm aluminum foil, with the result that about 0.1% of the electrons radiated a high-energy photon. The main electron beam was deflected into a heavily shielded beam dump. The post-bremsstrahlung electrons were momentum analyzed in an inclined pole magnetic spectrometer and were detected on the focal plane in a 32 channel plastic-scintillator hodoscope. With an 88.0-MeV electron beam, photons of energies between 63.3

and 71.1 MeV were tagged. The photons exited the spectrometer vacuum system and passed through a set of collimators, which limited the angular divergence of the photon beam to 33 msr (i.e., a radius of 3 cm at the downstream end of the target.) The tagging rate per focal counter was approximately 10^5 s^{-1} . At this tagging rate the trigger rate in the large solid-angle detector was $1.2 \times 10^3 \text{ s}^{-1}$, and the coincidence rate with the monochromator was 200 s^{-1} , the practical limit of the data acquisition system. Summing over the entire focal plane, the total tagged-photon flux used in this experiment was approximately $1.7 \times 10^6 \text{ s}^{-1}$.

The photon flux was determined in an auxiliary measurement. A 25.4-cm-diameter, 30.5-cm-long NaI(Tl) spectrometer was placed directly in the photon beam at greatly reduced intensities. To limit the rate in the crystal, the total rate in the focal plane was reduced to about 600 s^{-1} . For each electron counter the number of electrons N_i^e was counted, and a pulse-height spectrum of the photons detected by the crystal in coincidence with these electrons was collected. The pulse-height spectrum was integrated to determine the number of coincident photons N_i^γ . From tabulated attenuation coefficients the crystal was calculated to be 99.9% efficient for photon detection at 70 MeV. The tagging efficiency ϵ_i was given by the ratio N_i^γ/N_i^e . The tagging efficiency, averaged over the entire focal plane for the conditions of this experiment was $(51.4 \pm 1.0)\%$. The tagging efficiency was measured periodically, and the variation in these measurements was taken to be the systematic error in the determination of the photon flux.

B. Large solid-angle detector

The large solid-angle (LASA) detector was designed for photodisintegration measurements of light nuclei at photon energies up to 100 MeV. It has been used for a measurement of the cross section for deuteron photodisintegration.¹⁸ Since the LASA detector and associated electronics have been described previously,¹⁹ only a brief description is given here. The detector is shown schematically in Fig. 1. The target is at the center of the detector, and it is surrounded by a wire chamber consisting of three concentric levels of wires. The wires run parallel to the detector axis. Surrounding the wire chamber are two layers of plastic scintillators. These layers are broken up into eight planar sections, forming an octagonal cross section. The inner layer, used for the ΔE measurement, is 3 mm thick. The outer layer, used for the E measurement, is 25 mm thick. The ΔE - E combination is also used for particle identification.

The photon beam is directed down the central axis of the detector. Photodisintegrations in the target gas generate charged particles, most of which pass through the thin-target vessel wall and into the wire chamber volume. As the particles pass through each successive wire level, signals are registered in the nearby wires. From these signals both the hit position and the energy loss of the

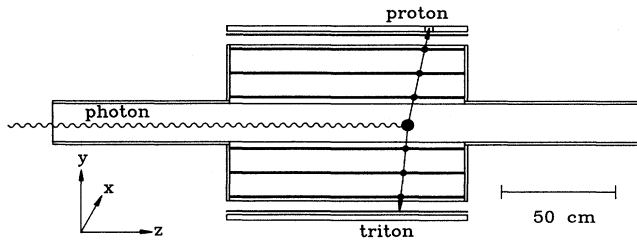


FIG. 1. Vertical section through the LASA detector axis, showing the trajectories of a typical ${}^4\text{He}$ photodisintegration event. The open circles represent the hits generated by the charged particles when they pass through each of the three cylindrical wire layers, and the block represents the detection of the proton in the scintillator $\Delta E, E$ shell.

particle in each layer are determined. Finally, the particle enters the thin scintillator, and, if it has sufficient energy, it passes through the thin into the thick scintillator. Both position and energy information are obtained from each $\Delta E-E$ pair.

Figure 1 shows a typical ${}^4\text{He}(\gamma, p){}^3\text{H}$ event in the detector. The proton makes a hit in the three wire levels, in the ΔE scintillator, and in the E scintillator, where it stops. The more massive triton, having less energy, leaves hits in the three wire levels, and stops in the ΔE scintillator. Note that the opening angle between the two tracks is only slightly less than 180° , since the momentum carried by the photon is small. Particles, produced in the target at laboratory polar angles between 16° and 164° with respect to the detector axis, can make a track that passes through all three wire layers and hits the thin scintillator.

C. Data acquisition

The event trigger is derived from the thin scintillators. The analog signals from the ends of each scintillator are discriminated, and these outputs are delivered to meantimers. The mean timer produces an "and" of the two ends of a scintillator. Due to attenuation in the scintillators the effective threshold of the meantimer is position dependent, higher for hits near the ends. The analog signals from the ends of each scintillator are also summed and then discriminated. The effective threshold for the sum discriminator is also position dependent, higher for hits near the center. The effective threshold of the "and" of the sum discriminator and the meantimer, when the thresholds are properly set, is fairly uniform along the length of the scintillator. The "or" of all eight thin scintillators is the event trigger.

The signals from the wire ends are fed into preamplifiers mounted directly on the chamber. The wire chamber is operated in proportional mode at modest gain. A typical proton track, averaged between the two ends of wire, produces 1 pC of collected charge and a 50 mV pulse at the preamplifier output. Such a pulse delivers 100 pC

within the gate of the ADC's connected to the ends. The rms noise from the preamplifiers is at the level of 1 pC. While this noise makes a negligible contribution to the energy resolution of the wires, it limits the position resolution of the wires to about 1.2 cm rms.

A network of three computers is used for data acquisition. One LSI-11/73 computer is devoted to the single task of servicing interrupts and filling buffers of data. Each time a data buffer is filled, it is passed to a second LSI-11/73 over an intercomputer data link. The second computer logs the data to magnetic tape and performs experimental control functions. The data buffers are also passed to a third computer, a VAXstation II, on which analysis is performed. The analysis software maintains hundreds of updating histograms and scatter plots with which the operation of the detector is monitored. The distributed processor configuration required distributed software. A software environment was created where many separate programs, each devoted to one particular aspect of data acquisition, can run currently and share data through a well defined interface. The VAXONLINE package from the Fermilab Online Computing Department²¹ provided this environment for the VAXstation. A similar package was developed for the LSI-11.²²

III. THE EXPERIMENT

A. Electromagnetic background

The data for this experiment were taken over a period of 35 hours, during which time approximately 1.3×10^7 events were logged to tape. Most of these events were not due to nuclear photodisintegration. In fact, the major obstacle to the success of this measurement was the electromagnetic background in the LASA detector. Careful collimation of the photon beam and tuning of the event trigger enhanced the signal-to-background ratio to the level of 0.3%: only one out of 300 event triggers corresponded to a coincident photodisintegration event. The dominant part of the background was found to be electrons and positrons, originating from photon conversions upstream of the detector, which passed through the scintillators at very shallow angles. The relative importance of the random background is illustrated in the typical timing spectrum shown in Fig. 2.

B. Trigger threshold

The trigger was chosen for maximum proton detection efficiency. For the photon energy of this experiment, protons emitted at forward and backward angles stopped in the thin scintillators. Thus, in order that these events not be excluded, the choice was made to trigger only on the thin scintillators. The discriminator thresholds were adjusted to produce an effective threshold that was nowhere higher than 1.8 MeV (equivalent electron energy or MeVee). Protons from ${}^4\text{He}(\gamma, p){}^3\text{H}$ at 90° produced

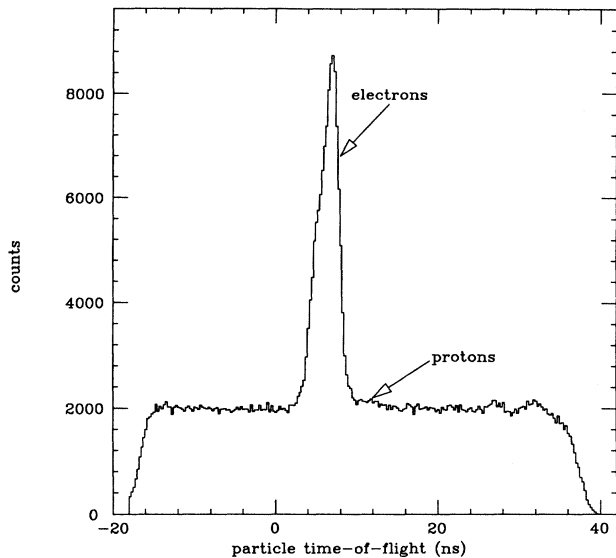


FIG. 2. Time-of-flight (TOF) spectrum for a sample of the complete data set for this experiment. The $t = 0$ point is the instant that the beam photon reached (or would have reached) the midpoint of the target. Most of the events are generated by particles with a TOF too small to be protons, and are identified as electromagnetic background associated with the beam. A small rise due to protons can be seen upon the flat background due to random coincidences between the LASA detector and the tagging spectrometer.

an average of 5 MeVee in the thin scintillators. Off-line data analysis showed that the threshold could have been as high as 3 MeVee without significant loss of efficiency.

C. Wire chamber operation

The wire chamber gas was a mixture of 90% helium and 10% methane. With this mixture low-energy heavily ionizing tritons could still be tracked through all three layers of the chamber. The wire gain with this mixture is not well understood. Several studies of the dependence of gain upon high voltage for different mixtures were done with a small prototype chamber. Observation of the gain at a fixed value of high voltage revealed large drifts over a period of several days. Anomalous gain in chambers operating with helium-methane mixtures has also been observed elsewhere.²³

Because the wire chamber gain was not constant, an adjustment had to be done during data analysis. During the initial setup of the LASA detector, the pulse-height spectrum from each of the three wire levels was generated, and the high voltages on each level were adjusted to match the gains. Periodic adjustments were made to the high voltages throughout the run to keep the gains near the initial setting. The gradual gain shifts which occurred took place on all three levels, so that they always stayed roughly equal.

One very surprising anomaly in the wire chamber gain

was uncovered during the data reduction. Up to that point it had been assumed, due to the cylindrical symmetry of the chamber and the fact that a common high voltage was delivered to each level, that all of the wires on a given level would have the same gain. It was discovered in the data analysis that the gain of an individual wire had a linear dependence on the vertical height of the wire in the chamber. On the outer layer the gain of the top wires was about a factor of 2 greater than the gain of the bottom wires. This behavior had not been observed when the chamber had been operated with an argon-helium mixture. The behavior was traced to a small leak in the seam of the mylar window which happened to be at the bottom of the chamber. A small amount of air leaking into the chamber from the bottom produced the variation of wire gain with wire height. This variation was very regular and was corrected for in the data analysis.

IV. DATA ANALYSIS

The raw data contained electromagnetic background events, cosmic-ray events, other background events, and helium photodisintegration events, all of which satisfied the trigger condition of a hit in at least one of the thin scintillators with an energy deposition over 2 MeVee. The goal of the data analysis was to identify the events arising from ${}^4\text{He}$ disintegration and to obtain the cross section. In fact, the experiment has obtained a reliable measurement of only the ${}^4\text{He}(\gamma, p){}^3\text{H}$ channel. The detector was not sensitive to the ${}^4\text{He}(\gamma, n){}^3\text{He}$ channel, since the range of the ${}^3\text{He}$ particle from the reaction was too small to trigger the scintillators, and since the neutron could not be tracked through the chamber, even if the thin scintillator were triggered. Events from the other two-body channel, ${}^4\text{He}(\gamma, {}^2\text{H}){}^2\text{H}$, were accepted, along with any events from the reactions, ${}^4\text{He}(\gamma, pn){}^2\text{H}$ and ${}^4\text{He}(\gamma, ppnn)$, with protons of sufficient energy to satisfy the trigger condition.

In the initial data reduction a few elementary cuts were made, which rejected about 98% of the background events and improved the signal-to-noise ratio from 1:300 to approximately 1:6. Repeated analysis passes were then made over the reduced data to find the best thresholds for the final cuts, and to estimate the associated uncertainties. The events were then accumulated into histograms. The contributions to these histograms from random coincidences were subtracted, and the efficiency correction and the overall normalization were applied to obtain the differential cross section.

A. Data translation

For convenience in the subsequent analysis, the raw ADC and TDC values were converted into the properly corrected time (ns), position (cm), and pulse-amplitude (MeVee) values which they represented. The detector was calibrated by elastic proton-proton scattering at the Indiana University Cyclotron Facility (IUCF).¹⁹

B. Event selection

The selection of valid ${}^4\text{He}(\gamma, p){}^3\text{H}$ events involved rejection of electromagnetic, cosmic-ray, and other backgrounds, and discrimination from other helium disintegration channels. The selection was done for two types of events: events in which only the proton from ${}^4\text{He}(\gamma, p){}^3\text{H}$ was detected (one-track events) and events in which both the proton and the triton from ${}^4\text{He}(\gamma, p){}^3\text{H}$ were detected (two-track events.) These two analyses were carried out because, although the identification of two-track events was completely unambiguous, the acceptance for one-track events was greater. The cross sections obtained from the two analyses must agree in overlapping regions of acceptance.

C. Analysis of wire chamber data

The wire chamber pulse height can effectively discriminate against background, but the path length in the wire cell must be taken into account. Electrons pass through the wire chamber at shallow angles, making long tracks in each of the wire levels. Thus the low specific ionization of the electrons is offset by their longer path length in the wire cell, and pulses are produced which are similar in magnitude to those from heavily ionizing protons passing through the wire cell at 90° . The path length is determined from the direction of the particle track. Thus particle tracks must be found and fitted. Then the pulse amplitude dE can be multiplied by the sine of the track angle to obtain dE/dx , which is independent of angle.

The search for track candidates involves identifying all the sets of three wire chamber hits, one hit on each level, which lie reasonably close to a straight line intersecting the target region. Furthermore, it is convenient to distinguish between *primary* tracks, which have a scintillator hit, and *secondary* tracks, which do not. (Almost all tritons make secondary tracks.) All events that fail to make a hit in all three wire levels are excluded from the analysis. (A correction must be applied later in the analysis to account for the events that have been missed for this reason.) The collinearity of the hits is first examined by projecting them onto a plane perpendicular to the detector axis (the x - y plane, with the detector axis in the z direction.) The (x, y) coordinates of each hit are obtained, and a linear least-squares fit is performed. If the χ^2 of the fit is within preset bounds, the candidate track passes on to be fitted in the other projection (the r - z plane), otherwise it is rejected.

The standard deviations of the hit coordinates, which are used in the track fitting algorithm, are adjusted until the χ^2_{xy} spectrum is consistent with the χ^2 distribution with one degree of freedom, and the χ^2_{rz} spectrum is consistent with a χ^2 with two degrees of freedom. The additional degree of freedom in the r - z fit is introduced by including the z -coordinate of the plastic hit in the fit. The final choices are as follows:

$$\begin{aligned} \text{wire coordinates : } \sigma_x = \sigma_y = 0.4 \text{ cm} \\ \sigma_z = 0.9 + \left(\frac{0.3 \text{ keV}}{\delta E} \right) \text{ cm} , \\ \text{plastic coordinate : } \sigma_z = 2.4 \text{ cm} . \end{aligned}$$

The event vertex position is also calculated from the particle track. Since the beam is confined to the region near the detector axis, a cut on the radial coordinate of the vertex position can be made without losing photo-nuclear events. This cut is very efficient for eliminating cosmic ray events, and some electrons are eliminated as well.

Since the amplitudes of the wire hits on all three levels are independent measurements of dE/dx , there are actually three dE/dx values from the wire chamber for each particle track. These values could be averaged, but it was a surprise to discover that the minimum value of the three provided greater discrimination between electrons and heavy particles. The minimum dE/dx from the wire chambers will be referred to simply as the wire dE/dx . The wire dE/dx of the primary track for a sample of events is shown in Fig. 3. There is good separation between electrons and heavy particles. The final wire dE/dx cut was placed at 1.0 keV/cm as indicated in the figure.

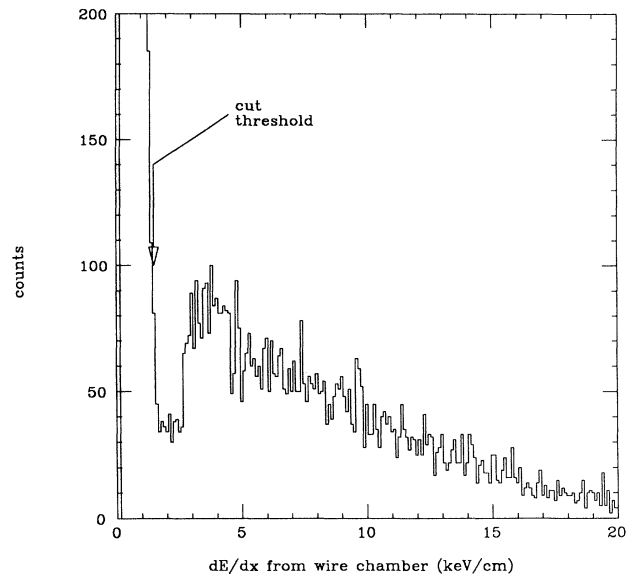


FIG. 3. Histogram of dE/dx in the wire chamber of all tracks that could be fitted from an unreduced sample of events. The peak at low dE/dx corresponds to the dominant peak in Fig. 2, and is identified as electrons. Above this peak, which contains over 90% of all tracks in the unreduced event sample, lie the heavier ionizing tracks that correspond to protons, deuterons and tritons from photodisintegration events. One of the criteria for identifying a photodisintegration event was a wire dE/dx greater than 1.5 MeV, as indicated by the cut threshold.

D. Analysis of scintillator data

The next cut is a threshold on the amplitude of the pulses from the plastic scintillators. There are two possible cuts: one on the dE/dx in the thin plastic scintillator and one on the total E deposited in the thin and thick scintillators. A dE/dx measurement is available, if the particle penetrated through the thin scintillator into the thick scintillator before it stopped. It is defined as the amplitude in MeVee divided by the path length through the thin scintillator. A dE/dx measurement is available for most of the protons, and it can be used in a similar way as the wire dE/dx to reject electrons. A plot of dE/dx from the scintillators is shown in Fig. 4, which includes all events which passed the previous cuts. A measurement of dE/dx from the scintillators is not available for tritons, since they do not make it through the thin scintillator. The arrow in the figure indicates where the final cut was placed. The cut threshold at 8 MeV/cm is below the point at which a significant number of protons begin to be lost.

The total energy deposited in the scintillators is shown in Fig. 5 for all events which passed previous cuts. The total E is taken from the sum of the amplitudes in the thin and thick scintillators. In the case of events that have more than one primary track, e.g., when both the proton and the triton make pulses in the plastic, only the one with the larger total E is histogrammed. Thus Fig. 5 can be considered as a sum spectrum of protons

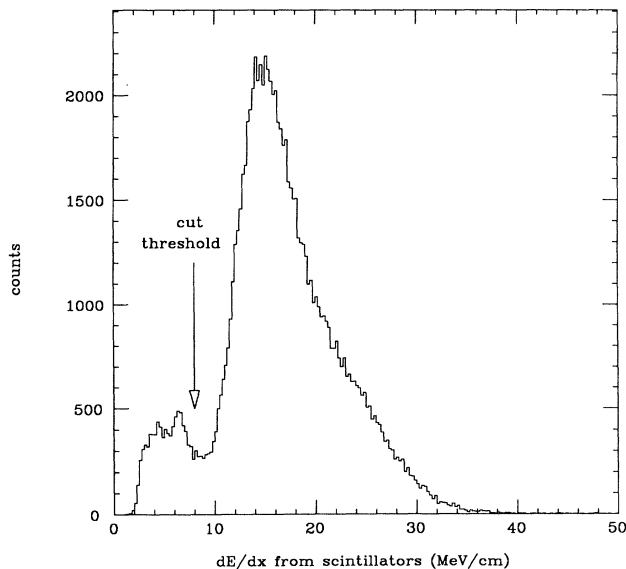


FIG. 4. Histogram of the dE/dx in the plastic scintillator, for a sample of tracks that passed the wire dE/dx cut. The dominant peak corresponds to protons, and the secondary peak at low-energy loss is due to minimum-ionizing tracks still present in the sample after the wire dE/dx cut. A rejection of all tracks with a dE/dx in the plastic scintillator below 8 MeV further purifies the sample.

from photodisintegration, plus miscellaneous tracks from background events. The peak centered at 25 MeVee is identified as the two-body (γ, p) peak. The rest of the spectrum is from protons and deuterons from other channels, and from the remains of the electron background.

The choice of a threshold cut on total E is rendered ambiguous by the long tail on the low side of the peak. This tail is due to the fact that some protons escape through the sides or ends of the scintillator, before they deposit all of their energy. The choice is made, in the calculation of the geometric acceptance, to require that a particle track must have at least 0.8 cm of path length in the scintillator before it escapes, if it is to be accepted as within the detector geometric limits. For a proton of 35 MeV incident energy, this implies a minimum energy loss of 15 MeV in the plastic, corresponding to 13 MeVee. Therefore, the cut threshold on the total energy E deposited in the plastic scintillators was placed at 13 MeVee. The resolution of the total energy deposited in the plastic scintillators is 15% FWHM.

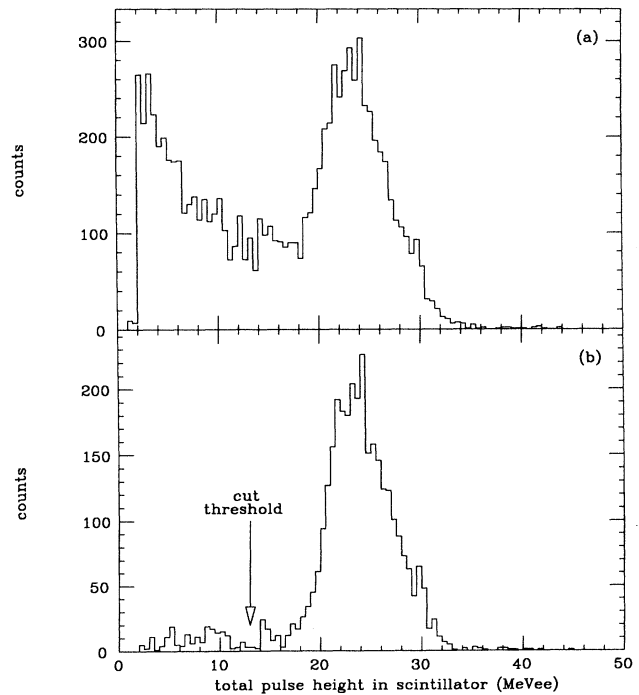


FIG. 5. Histogram of the total energy deposited in the plastic scintillator for a sample of tracks that passed the dE/dx cuts in the wires and plastic scintillators. (a) E of the dominant track in each event, regardless of whether other tracks were also found. (b) E of the dominant track in each event in which another heavily ionizing track was also found, which satisfies together with the dominant track the kinematic constraint of a two-body photodisintegration reaction. The prominent peak at high energy corresponds to two-body photodisintegrations, and the tracks with lower E in (a) show the presence of three-body and four-body photodisintegrations that are also present in the reduced sample.

E. Two-track and one-track events

Discrimination between two-body events and multi-body events can be achieved by exploiting cuts based upon two-body kinematics; however, it is then necessary to analyze only events with two tracks. The first track must be a primary, and must pass all of the cuts described above. The second track is subjected to all cuts but the dE/dx and total E cuts from the plastic scintillators. Additional cuts are available from the track angles. The distribution of the difference, $\phi_1 - \phi_2$, in the azimuthal angle ϕ between the first and second track has a maximum at 180° , because kinematics requires the tracks to be collinear in the x - y plane. This peak sits upon the broad distribution of three-body and four-body events, whose tracks are not kinematically confined to a plane. A similar requirement is made on the sum $\theta_1 + \theta_2$ of the polar angle θ between the two tracks. Applying cuts on θ and ϕ , the contamination in the final spectra from the three-body and four-body channels is reduced to 2.8% of the two-body channel.

For events with just one track, only the total energy measurement is available for identification of the two-body channel. With the modest energy resolution of the scintillators, the maximum energy protons from the multibody final states cannot be distinguished from the protons from the two-body final state. To separate the two-body final state from the multibody final states, peak shapes were found for the two spectra. Then by fitting these shapes to the measured spectra, the number of two-body events is identified. The peak shape for protons from two-body events at different energies and angles is obtained from the analysis of two-track events. As a check, the GEANT Monte Carlo program²⁴ was used to model the energy loss in the scintillators. A peak shape is then derived by convoluting the GEANT energy spectrum with a resolution function for monoenergetic protons, which was measured during the calibration experiment at IUCF. Good agreement is found with the peak shape from the two-track analysis. The peak shape for the multibody spectra is taken from a selection of events that required two noncollinear tracks in the detector. These two peak shapes are then used to find the number of protons in the one-track distribution that are due to the two-body final state. As shown below, the one-track and two-track analysis are in agreement in the angular region for which both have nonzero acceptance.

F. Random subtraction

Up to this point of the analysis, no use has been made of the information available from the monochromator. Virtually all of the events remaining after the above cuts have been performed are ${}^4\text{He}(\gamma, p){}^3\text{H}$ photodisintegration events. However, not all of these events correspond to gamma rays within the energy range of the tagger. (Thus the photon energy is not known.) The photon beam contains gamma rays of a continuum of energies, and many of the photodisintegrations arising from lower-

energy gamma rays generate random coincidences with the monochromator. The sample of true coincidences can be enriched by excluding all events outside of the region of the coincidence peak. A typical timing spectrum is shown in Fig. 2. The width of the timing window was chosen so that just over 99% of the ${}^4\text{He}(\gamma, p){}^3\text{H}$ events are included. While there is nothing to prevent the use of a wider window, the three-body and four-body events tend to fall outside of the peak, and the narrower window helps suppress them.

The procedure for subtracting random coincidences from the angular distribution depends upon the fact that a sample of random-coincidence events has the same composition, no matter from where it is drawn in the monochromator timing spectrum. The angular distribution of random events from a time window off the coincidence window is scaled by the ratio of the width of the coincidence window to the width of the random window. The true coincidence angular distribution is obtained by subtracting the one distribution from the other. The width of the randoms window was chosen to be as wide as possible in order to minimize the statistical error introduced by the random subtraction.

G. Geometric acceptance

The measured yield as a function of proton angle must be corrected for various detector efficiencies to obtain a differential cross section. The leading contribution to the overall efficiency of the LASA detector is the geometric acceptance, which accounts for the fact that the detector does not subtend a full 4π sr around the target. For a given track direction (θ, ϕ) , only a segment of the target is "active." A volume element of the target is said to be active for angles (θ, ϕ) , if a track extending from the volume element, pointing in direction (θ, ϕ) , passes through all three wire layers and penetrates a thin scintillator. At very forward and very backward angles, no volume of the target is active, and the acceptance is zero. At 90° all of the target contained inside the bounds of the chamber is active. The geometric acceptance function $\lambda_1(\theta)$ is defined as the length, in cm, of the active segment of the target. This function was evaluated by a Monte Carlo calculation, which respected the full geometric complexity of the detector.

The geometric acceptance function described above is constructed with the requirement of only a single-track; i.e., an event need only register one acceptable track to be counted. In the analysis of two track events, the ${}^4\text{He}(\gamma, p){}^3\text{H}$ channel is separated from the three-body and four-body breakup channels by counting only events with both a proton and a triton track. Adding the requirement of a second track specified by the appropriate two-body kinematics, a two-track geometric acceptance function $\lambda_2(\theta)$ was also evaluated by a Monte Carlo calculation.

The geometric acceptance functions $\lambda_1(\theta)$ and $\lambda_2(\theta)$ are shown in Fig. 6. Note that the two-track require-

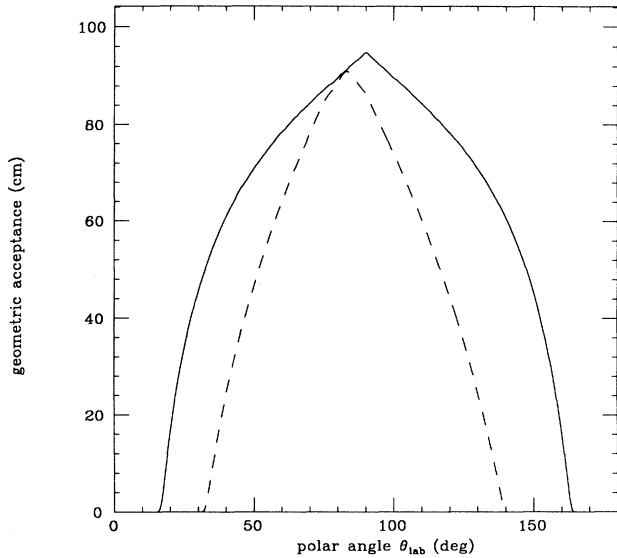


FIG. 6. Geometric acceptance function corresponding to the one-track analysis (solid curve) and the two-track analysis (dashed curve), as a function of the polar angle θ in the laboratory frame.

ment considerably contracts the range of angles which are accessible to the measurement.

H. Track and cut efficiencies

Throughout the analysis a quantitative determination of the acceptance efficiency of each cut for ${}^4\text{He}(\gamma, p){}^3\text{H}$ events has been made. These determinations were made so that the final result can be corrected, and a reliable absolute cross section can be obtained. The total efficiency function is composed of a product of independent efficiencies as $\varepsilon(\theta) = \varepsilon_0(\theta) \varepsilon_1 \varepsilon_2 \varepsilon_3 \dots$. The geometric acceptance function $\lambda(\theta)$ is not included in $\varepsilon(\theta)$. The geometric acceptance correction is included in the calculation of the target thickness.

The quantity $\varepsilon_0(\theta)$ represents the implicit requirement that both proton and triton must not be absorbed before they make complete tracks. To complete its track, a proton must reach the plastic annulus with enough remaining kinetic energy to pass the plastic total E cut. A triton is only required to penetrate wire level C to complete its track. Once these requirements are met, all losses are accounted for by the explicit cuts outlined in Secs. IV C–E. The function $\varepsilon_0(\theta)$ is evaluated by Monte Carlo.

Protons and tritons of the correct energy were injected by Monte Carlo simulation into the LASA detector from the axis of the target at a series of angles θ . The azimuth ϕ of the track was permitted to vary randomly. The great majority of the protons complete a track, as expected. A significant fraction of the tritons are lost in the wire chamber, mainly from hitting the wires. The

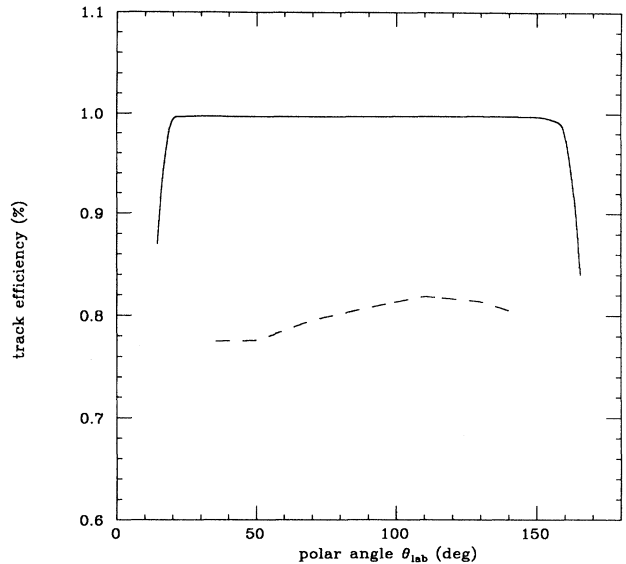


FIG. 7. Track efficiency function corresponding to the one-track analysis (solid curve) and the two-track analysis (dashed curve), as a function of the polar angle θ in the laboratory frame.

track efficiency $\varepsilon_0(\theta)$ is calculated as a function of the center-of-mass angle of the proton track. The resulting efficiencies for one-track and two-track events are shown in Fig. 7.

The efficiencies $\varepsilon_1 \varepsilon_2 \varepsilon_3 \dots$ associated with the remaining cuts should *a priori* be treated as functions of θ , similar to $\varepsilon_0(\theta)$. However, the cuts were imposed upon spectra which either had no angular dependence, or whose

TABLE I. Summary of the cuts imposed upon event parameters in order to suppress the presence of backgrounds in the final sample of photodisintegration events. The general cuts are used in both the 1-track and 2-track analyses, and the additional cuts are specific to the 2-track analysis.

General cuts	Inefficiency (%)
Track fit $\chi^2 \leq 20$ (both xy and rz projections)	0.1
Radius of event vertex $r \leq 6$ cm	1.7
Wire $dE/dx \geq 1.5$ keV/cm	0.3
Plastic scintillator $dE/dx \geq 8$ MeV/cm	0.4
Tagging coincidence timing cut	0.6
Total for general cuts	3.1
Additional cuts for two-track analysis	
$ \varphi_1 - \varphi_2 = 180^\circ \pm 6^\circ$	2.3
$(\theta_1 + \theta_2) = 167^\circ \pm 25^\circ$	0.6
Plastic scintillator $E \geq 6$ MeV	1.6
Total for two-track analysis	7.4

angular dependence had been removed, as in the case of the dE/dx cuts. Therefore, these efficiencies are treated as constants. The efficiency factors are given in Table I for each of the explicit cuts described in Secs. IV C–E. The numbers are taken directly from the acceptance plots that were obtained for each cut. The product of the efficiencies from Table I is 93.95%.

I. Normalization

The experimental angular distribution in the center-of-mass frame is related to the differential cross section by

$$Y(\theta_{c.m.}) = N\lambda(\theta_{c.m.})\varepsilon(\theta_{c.m.})\frac{d\sigma(\theta_{c.m.})}{d\Omega}\Delta\Omega(\theta_{c.m.}) \quad (1)$$

In this equation the normalization factor N is given by the product $\Phi\rho$, where Φ is the total number of tagged photons incident on the target, and ρ is the target density in atoms per cm^3 . Summed over the entire tagging interval from 63 to 71 MeV, the number of tagged photons Φ is 8.82×10^{10} . The target density is obtained from

$$\varrho = \varrho_{\text{STP}} \left(\frac{T_0}{T}\right) \left(\frac{P}{P_0}\right) \frac{N_A}{A}, \quad (2)$$

where ϱ_{STP} is the density of ^4He in g/cm^3 at standard temperature (T_0) and pressure (P_0), N_A is Avogadro's number, and A is the gram-atomic weight of ^4He . The actual temperature and pressure measured during the experiment are denoted by T and P , respectively. The geometric acceptance function $\lambda(\theta_{c.m.})$, introduced in Sec. IV G, represents the length of the target segment in cm from which $^4\text{He}(\gamma, p)^3\text{H}$ events at a proton angle θ are not excluded by the geometry of the LASA detector. Thus, the quantity $\rho\lambda$ has units of scatterers per cm^2 . The efficiency correction $\varepsilon(\theta_{c.m.})$ was discussed in Sec. IV H. The solid angle factor $\Delta\Omega(\theta_{c.m.})$ is $2\pi(\pi/n)\sin(\theta_{c.m.})$, where n is the number of angular bins. An added and important consideration in obtaining the differential cross section is the angular resolution of the detector. The effect of the angular resolution of the detector is removed from the measured yield $Y(\theta_{c.m.})$ by performing an angular deconvolution using an empirical parametrization of the angular resolution.

V. RESULTS

Two angular distributions were derived from the data, one from the one-track analysis and one from the two-track analysis. The angular distribution for the two-track analysis was more reliable, since the signature for a two-track event completely excluded three-body and four-body final states. However, the angular acceptance for the two-track events was smaller than for the one-track events. Thus the one-track analysis was needed to extend the angular distribution to extreme angles. Sepa-

rate analysis of the two types of events provided a check on systematic errors.

A. Two-track results

The two-track distribution was obtained first because these events were more easily identified. As described above, a cut was placed on the two tracks requiring that they satisfy two-body kinematics. Because of geometry, the two-track requirement limited the polar angle of the proton to the range from 35° to 140° . About 200 000 events satisfied the two-track requirement. A plot of the differential cross section and a fit to the data are shown in Fig. 8.

B. One-track results

The angular acceptance of one-track events extends from 20° to 160° . There were 130 000 events measured over the energy range from 63 to 71 MeV. A plot of the data is shown in Fig. 9. For comparison the two-track results are also indicated. The differential cross sections are listed in Table II.

C. Legendre fits and comparison of one-track and two-track data

The differential cross sections for the one-track and two-track angular distributions were fitted by the series

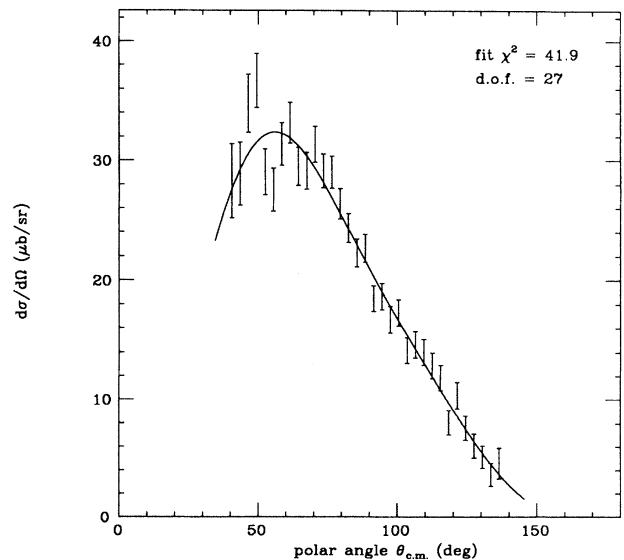


FIG. 8. Differential cross section for the summed energy window from 63 to 71 MeV for the two-track results, showing the data points with statistical errors, and the fit to a Legendre series up to $P_5(\cos\theta_{c.m.})$. The angular limits of the measurement are imposed by the limits of the two-track geometrical acceptance function.

$$f(\theta) = A_0 \left(1 + \sum_{n=1}^N a_n P_n(\cos \theta) \right), \quad (3)$$

where θ is the polar angle of the proton track in the center-of-mass frame, P_n was the Legendre polynomial of order n , and the coefficients A_0 and the a_n were determined by a fit to the data. To investigate the best place to truncate the Legendre expansion, a sequence of fits was performed, each one including an additional term in the series. The values of the coefficients that minimized the value of χ^2 were determined in the fitting procedure. Fits to the one-track and two-track data were made for the data integrated over the entire 8 MeV band of photon energy from 63 to 71 MeV and for the data divided up into four photon energy bins of 2 MeV each.

Considering the fit to the integral two-track data first, large values of χ^2 for $N \leq 2$ indicated that the $N = 3$ term was needed to get a reasonable fit to the data. The quality of the fit was further improved when the $N = 4$ term was included; however, when the fit was extrapolated beyond the angular range of the two-track data, i.e. to angles less than 30° or angles greater than 150° , the fit became negative, which was unphysical. To correct this problem, dummy data points of $0.3 \pm 1.0 \mu\text{b/sr}$ at 0° and $0.2 \pm 1.0 \mu\text{b/sr}$ at 180° were added to the data to ensure a positive cross section at forward and backward angles. With these constraints the net improvement in the value χ^2 then justified the inclusion of the $N = 4$ term, and a further decrease in the value of χ^2 was obtained when the $N = 5$ term was included. The fit parameters and χ^2 values for the two-track data reported in Table III are

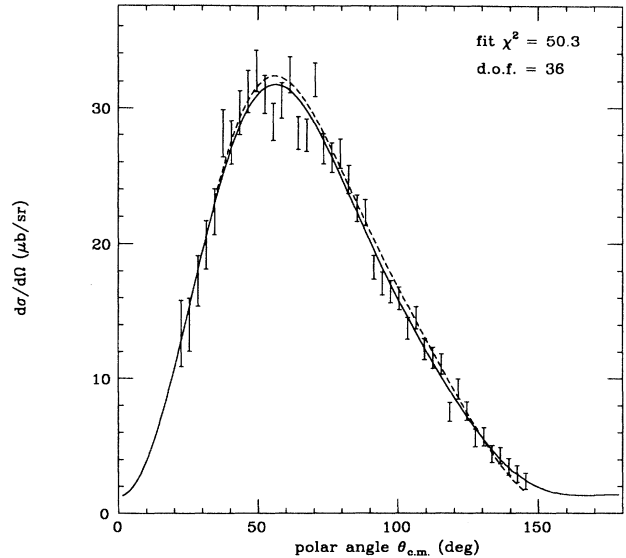


FIG. 9. Differential cross section for the summed energy window from 63 to 71 MeV for the one-track results, showing data points with statistical errors, and the fit (solid line) to a Legendre series up to $P_5(\cos \theta_{c.m.})$. The fit curve from the two-track analysis (Fig. 8) is superimposed as a dotted line for comparison.

those obtained with the constraints. However, the statistical uncertainties in the fit parameters are strongly dependent on the constraints imposed on the fit at 0° and 180° and are smaller than is warranted by the data themselves.

TABLE II. Experimental differential cross sections obtained from the one-track and two-track analyses, including all of the data from 63 to 71 MeV. The errors are statistical only.

Angle (c.m.) (deg)	One-track results ($\mu\text{b/sr}$)	Two-track results ($\mu\text{b/sr}$)	Angle (c.m.) (deg)	One-track results ($\mu\text{b/sr}$)	Two-track results ($\mu\text{b/sr}$)
22.5	13.4 ± 2.5		85.5	22.6 ± 1.0	22.3 ± 1.2
25.5	14.0 ± 2.0		88.5	22.3 ± 1.0	22.7 ± 1.2
28.5	17.2 ± 1.9		91.5	18.3 ± 0.9	18.5 ± 1.1
31.5	19.9 ± 1.8		94.5	17.1 ± 0.9	18.7 ± 1.1
34.5	22.3 ± 1.7		97.5	16.5 ± 0.8	16.7 ± 1.1
37.5	28.1 ± 1.8		100.5	15.9 ± 0.8	17.3 ± 1.1
40.5	27.4 ± 1.6	28.3 ± 3.1	103.5	13.7 ± 0.8	14.2 ± 1.1
43.5	29.6 ± 1.6	28.9 ± 2.6	106.5	14.5 ± 0.8	14.7 ± 1.1
46.5	31.2 ± 1.6	34.8 ± 2.4	109.5	12.2 ± 0.8	14.0 ± 1.1
49.5	32.7 ± 1.5	36.7 ± 2.3	112.5	11.6 ± 0.8	12.9 ± 1.1
52.5	31.0 ± 1.4	29.0 ± 1.9	115.5	11.1 ± 0.8	11.9 ± 1.1
55.5	29.0 ± 1.4	27.5 ± 1.8	118.5	7.5 ± 0.7	8.1 ± 1.0
58.5	30.6 ± 1.3	31.4 ± 1.8	121.5	9.2 ± 0.8	10.4 ± 1.1
61.5	32.4 ± 1.3	33.2 ± 1.7	124.5	7.6 ± 0.7	7.6 ± 1.0
64.5	28.1 ± 1.2	29.5 ± 1.6	127.5	5.6 ± 0.7	6.1 ± 1.0
67.5	28.0 ± 1.2	29.1 ± 1.5	130.5	5.7 ± 0.7	5.1 ± 1.0
70.5	32.1 ± 1.2	31.3 ± 1.5	133.5	4.4 ± 0.6	3.6 ± 1.0
73.5	27.0 ± 1.1	29.1 ± 1.4	136.5	4.3 ± 0.6	4.6 ± 1.3
76.5	26.3 ± 1.1	29.0 ± 1.3	139.5	3.5 ± 0.6	
79.5	26.6 ± 1.1	26.4 ± 1.3	142.5	2.9 ± 0.6	
82.5	24.7 ± 1.0	24.4 ± 1.2	145.5	2.4 ± 0.6	

A more meaningful fit was obtained to the one-track data, which extended to more forward and backward angles. For the one-track data the quality of fits for $N \geq 2$ was also investigated. Again the inclusion of terms up to $N = 5$ was justified by the improvement in the value of χ^2 . Unlike the two-track data, no constraints were used in the analysis of the one-track angular distribution for the data integrated over the full 8-MeV photon energy range. For the data divided into four 2-MeV bins the constraints were again used. These results are listed in Table III. The statistical and systematic errors are listed separately.

D. Systematic errors

In the analysis of errors consideration must be given to the precision of each quantity that enters into the calculation of the cross section. In Eq. (1) each quantity is shown separately. The errors on $Y(\theta_{c.m.})$ are strictly statistical. The uncertainties on the photon flux Φ , the efficiency ε , and the geometric acceptance λ are the sources of systematic error. Systematic errors introduced while making cuts for event selection are included in errors on the efficiency.

The total flux of tagged photons is calculated by multiplying the focal plane scaler counts by the tagging efficiency. The tagging efficiency was measured eight times

during the course of the run. The errors in the measurement are derived from the statistics of the calibration runs, which are about 2% per run. The tagging efficiency calibration data are consistent with a constant tagging efficiency throughout the run, with the exception of two counters whose data indicated a one standard deviation fluctuation of about 5%. A typical uncertainty of 1% in the tagging efficiency is obtained for each counter, while the figure for the counters with the 5% fluctuation is 2%. An estimated systematic uncertainty of 1% is assigned to the total photon flux, applicable to the spectra summed over sets of eight counters, as well as the overall spectrum summed over all 32 counters.

The next sources of systematic error to be considered are the geometric acceptance functions $\lambda_i(\theta_{c.m.})$. The uncertainty on this quantity is related to how precisely the positions of all of the LASA detector components are known. Shifting counter dimensions within reasonable limits and repeating the Monte Carlo calculation of λ_2 gives a net change in λ_2 of about 1% in the angular range between 36° and 141° . The percentage uncertainty becomes quite large outside of these angular limits, where the absolute value of λ_2 is very small, so data from these bins were excluded from the angular distribution. Thus the error on λ_2 is estimated to be 1%. The error in λ_1 over the same angular range as λ_2 was also assumed to be 1%.

TABLE III. Summary of the final cross-section parameters obtained by a fit of a Legendre series to the differential-cross section data. The statistical errors are listed along with the parameters, and the systematic errors that apply to each column are shown at the bottom. The quality of the fits is indicated by the χ^2 per degree of freedom (d.o.f.) listed in the rightmost column.

Two-track sample							
Fit coefficients with statistical errors							
E_γ (MeV)	A_0	a_1	a_2	a_3	a_4	a_5	$\chi^2/\text{d.o.f.}$
63 - 71	17.59 ± 0.25	0.80 ± 0.03	-0.63 ± 0.04	-0.62 ± 0.03	-0.32 ± 0.03	-0.17 ± 0.04	42.0/29
64.0	19.16 ± 0.50	0.78 ± 0.05	-0.71 ± 0.06	-0.61 ± 0.05	-0.24 ± 0.06	-0.17 ± 0.08	24.5/29
65.8	18.97 ± 0.43	0.75 ± 0.05	-0.62 ± 0.05	-0.61 ± 0.05	-0.33 ± 0.05	-0.15 ± 0.08	33.2/29
67.8	17.15 ± 0.44	0.88 ± 0.05	-0.63 ± 0.05	-0.55 ± 0.05	-0.32 ± 0.05	-0.33 ± 0.07	39.5/29
70.0	15.08 ± 0.39	0.84 ± 0.05	-0.60 ± 0.06	-0.73 ± 0.06	-0.33 ± 0.06	-0.11 ± 0.08	28.1/29
Systematic errors on fit coefficients							
	A_0	a_1	a_2	a_3	a_4	a_5	
	± 0.60	± 0.08	± 0.03	± 0.06	± 0.10	± 0.04	
One-track sample							
Fit coefficients with statistical errors							
E_γ (MeV)	A_0	a_1	a_2	a_3	a_4	a_5	$\chi^2/\text{d.o.f.}$
63 - 71	$17.18 \pm .19$	$0.79 \pm .03$	$-0.60 \pm .04$	$-0.65 \pm .05$	$-0.32 \pm .05$	$-0.15 \pm .05$	50.3/36
64.0	$18.89 \pm .33$	$0.76 \pm .03$	$-0.67 \pm .04$	$-0.64 \pm .04$	$-0.29 \pm .04$	$-0.11 \pm .04$	34.1/38
65.8	$18.15 \pm .32$	$0.79 \pm .03$	$-0.61 \pm .04$	$-0.62 \pm .04$	$-0.34 \pm .04$	$-0.17 \pm .04$	39.1/38
67.8	$16.94 \pm .30$	$0.82 \pm .03$	$-0.59 \pm .04$	$-0.60 \pm .04$	$-0.36 \pm .04$	$-0.22 \pm .04$	48.3/38
70.0	$16.14 \pm .28$	$0.83 \pm .03$	$-0.59 \pm .04$	$-0.73 \pm .04$	$-0.34 \pm .04$	$-0.10 \pm .04$	40.8/38
Systematic errors on fit coefficients							
	A_0	a_1	a_2	a_3	a_4	a_5	
	± 0.58	± 0.04	± 0.03	± 0.05	± 0.05	± 0.05	

The remaining source of systematic error is the efficiency function $\epsilon(\theta)$. This function is a product of several efficiency functions, which were discussed above in Sec. IV H. The systematic uncertainty on the track efficiency function ϵ_o is 2%. The efficiencies associated with the explicit cuts were carefully quantified and listed in Table I. An uncertainty of no more than 10% in the magnitude of the correction should be applied to any one of these. Thus the systematic error due to the explicit cuts is no more than 0.3% for the one-track data and 0.7% for the two-track data. One bad wire out of 128 on the B level was found to be unreliable, so a 1% systematic uncertainty is included for this wire.

The complete list of systematic uncertainties that have been compiled is given in Table IV. Adding the errors in quadrature, the net systematic uncertainty is found to be 3.1% for the one-track analysis and 3.2% for the two-track analysis.

Any set of Legendre coefficients resulting in a curve that is contained within the one standard deviation band of systematic error on the differential cross section is consistent with the results of this experiment. An approximation to the systematic error on the Legendre coefficients can be obtained by varying each one independently until the fitted curve crosses the one standard deviation boundary of the systematic uncertainty. The results are given in Table III. These errors apply to all of the angular distributions, regardless of their statistical errors. The total uncertainty can be estimated by summing the statistical and systematic errors in quadrature. This yields a value of 5% for the A_0 coefficient, and hence for the total cross section. As was reported in Sec. IV E, a 2.8% contribution from the three-body and four-body photo-disintegration channels remains in the final spectra for the two-track data. This may be corrected by subtracting 2.8% from the A_0 coefficient. Making this correction, and collecting all of the errors together, the final results are given in Table III.

TABLE IV. Summary of the sources of systematic uncertainties, along with the percent error assigned to each effect. The totals for the one-track and two-track analysis are obtained by summing the individual contributions in quadrature.

Common sources of systematic uncertainty	
Detector acceptance to protons	2.0%
Tagging efficiency	1.0%
Bad wire on level B	1.0%
Systematics specific to one-track analysis	
Subtraction of three- and four-body contribution	1.9%
Total for one-track analysis	3.1%
Systematics specific to two-track analysis	
Subtraction of three- and four-body contribution	0.5%
Detector acceptance to tritons	2.0%
Two-body kinematics cut	0.3%
Total for two-track analysis	3.2%

E. Comparison with other experiments

Measurements of the cross section for ${}^4\text{He}(\gamma, p){}^3\text{H}$ and the inverse reaction ${}^3\text{H}(p, \gamma){}^4\text{He}$ were reviewed in 1984 by Cameron.²⁵ Almost all previous measurements of these reactions are at lower ($E_\gamma < 50$ MeV) or at higher ($E_\gamma > 100$ MeV) energies than the energy of the present experiment. The exceptions have been bremsstrahlung experiments, using cloud chamber techniques, with photon energies from threshold to approximately 170 MeV. Two extensive data sets are due to Gorbunov, which are summarized in his review article¹² and to the Kharkov group.¹⁶ A comparison can be made both to the total cross section and the angular distributions obtained in these experiments.

1. Total cross section

There is at first sight some difficulty in the total cross section comparison. For photon energies between 42.5 and 77.5 MeV Gorbunov tabulates the total cross section for ${}^4\text{He}(\gamma, p){}^3\text{H}$ in 5 MeV intervals (see his Table 7). At 67.5 MeV Gorbunov reports the value of $110 \pm 30 \mu\text{b}$. This value appears to be in disagreement with the value of $217.8 \pm 7.7 \mu\text{b}$ found in this experiment (see our Table III) for the energy interval 63 to 71 MeV. The Gorbunov value, however, appears much lower than the values he reports at adjacent energy bins.

The total cross section is also reported by the Kharkov group. Unfortunately, a tabulation of these data has not been published, but from the graphical values (see their Fig. 1 and Fig. 7), a value at 67.5 MeV of $180 \pm 30 \mu\text{b}$ can be obtained, in better agreement with the value found in this experiment. The total cross sections for ${}^4\text{He}(\gamma, p){}^3\text{H}$ from threshold to approximately 170 MeV reported by Gorbunov and the Kharkov group are generally in rather good agreement with one another. It is reasonable to conclude then that the one low value at 67.5 MeV reported by Gorbunov is not significant.

A further check on the overall normalization of these experiments can be obtained from a comparison to the ${}^4\text{He}(\gamma, p){}^3\text{H}$ total cross-section measurement by the Frascati group¹⁷ at several energies up to 58.1 MeV. The Frascati group used a monochromatic photon beam and a large acceptance detector. At 58.1 MeV the Frascati cross section of $440 \pm 10 \mu\text{b}$ is in reasonable agreement with the value of $390 \pm 50 \mu\text{b}$ from Gorbunov and the value of $330 \pm 30 \mu\text{b}$ from the Kharkov group. Better agreement is found at lower energies, although below 30 MeV there are larger differences among the experiments. Since the total cross section decreases by a factor of 3 between 30 and 50 MeV, the energy averaging of all the experiments must be very accurately considered in a more detailed comparison.

2. Angular distribution

Angular distributions have also been reported by Gorbunov and the Kharkov group. To increase the statistical

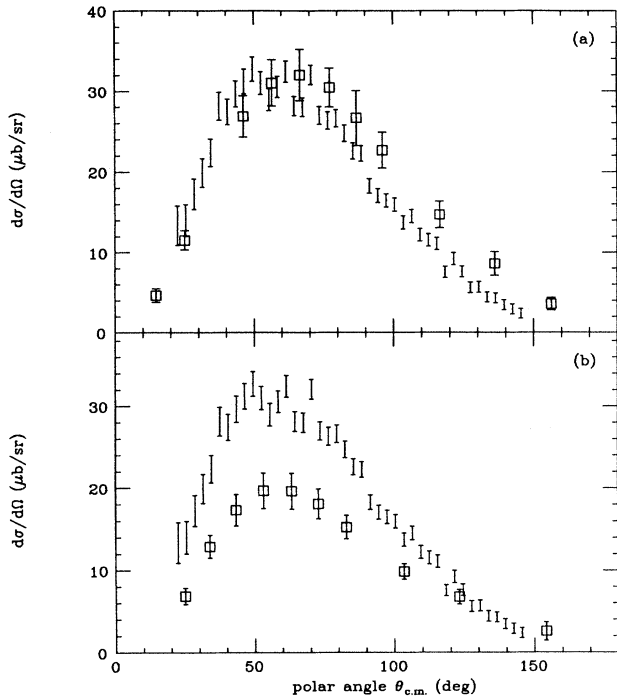


FIG. 10. Comparison of the present data (bars) at a mean energy of 64 MeV with the data (squares) from the Kharkov group¹⁵ at 60 MeV in part (a) and at 80 MeV in part (b).

precision of his differential cross sections, Gorbunov reported results for photon energies averaged between 36 and 65 MeV and for photon energies averaged between 65 and 170 MeV. With better statistical precision the Kharkov group has been able to report results at 60 and 80 MeV.¹⁵ We compare our result to the Kharkov measurement in Fig. 10. There is no large disagreement between the two experiments.

Gorbunov and the Kharkov group have fitted their differential cross sections, not with Legendre polynomials, but with an alternative, but equivalent expansion. This expansion allows a useful interpretation of the angular distribution under certain assumptions that are very reasonable for photodisintegration of ⁴He. These assumptions are that the photon multipolarity is limited to *E*1, *E*2, and *M*1, and that the nuclear matrix elements of

the electric multipoles to final states with channel spin one are negligible. The expansion is given in terms of parameters *A*, *β*, *γ*, *δ*, and *ε*,

$$\frac{d\sigma}{d\Omega} = A(\sin^2 \theta + \beta \sin^2 \theta \cos \theta + \gamma \sin^2 \theta \cos^2 \theta + \delta + \epsilon \cos \theta) \quad (4)$$

Then under the above assumptions the parameter *A* is due to the incoherent sum of the *E*1, *E*2, and *M*1 multipoles, the parameter *β* is due to the interference of *E*1 and *E*2 multipoles, the parameter *γ* is due to the *E*2 multipole alone, the parameter *δ* is due to the *M*1 multipole alone, and the parameter *ε* is zero.²⁶ In fact, the *ε* parameter has not been included in the fits reported by Gorbunov or the Kharkov group. Nevertheless, some comparison can be made between the two data sets by transforming the Legendre coefficients obtained in the present experiment to the greek coefficients. The results from Table III were averaged together and transformed to the greek coefficients, treating statistical and systematic uncertainties separately in propagating the errors. The results are given in Table V, along with the Gorbunov values. A fit to the same parametrization can be made for the angular distributions from the Kharkov group reported by Gurev. The results of this fit are shown in Table VI. (For these fits χ^2 per degree of freedom is less than 0.1, which suggests that the errors are not meaningful. If Gurev has reported fitted cross sections with correlated errors, a small χ^2 would be obtained.)

Although the angular distributions reported by Gorbunov and by the Kharkov group are not at precisely the same energy as the angular distribution reported in this experiment, it is still apparent from the tables and the graphs that there is reasonable agreement among the experiments. The angular distribution parameters then show evidence of *E*1-*E*2 interference from the large *β* coefficient, considerable *E*2 strength from the large *γ* coefficient, little *M*1 strength from the small *δ* coefficient, and little *S* = 1 contribution from the small *ε* coefficient.

F. Comparison with calculations

There are three major theoretical calculations which can be compared with these data. These are the quasi-deuteron model calculation of Noguchi and Prats,²⁰ the

TABLE V. Fit parameters obtained using the expansion of Eq. (3) rather than the Legendre expansion, shown for the present data in comparison with those of Gorbunov.¹² The present data are shown as parameter \pm statistical error \pm systematic error.

Coefficient	Gorbunov 36-65 MeV	Present results 63-71 MeV	Gorbunov 65-170 MeV
<i>A</i>	39.8 \pm 3.1	18.90 \pm 1.25 \pm 1.00	6.5 \pm 0.9
<i>β</i>	1.06 \pm 0.14	1.48 \pm 0.15 \pm 0.10	1.29 \pm 0.27
<i>γ</i>	0.28 \pm 0.29	1.27 \pm 0.11 \pm 0.16	-0.29 \pm 0.42
<i>δ</i>	0.02 \pm 0.03	0.07 \pm 0.07 \pm 0.05	0.10 \pm 0.07
<i>ε</i>		0.13 \pm 0.07 \pm 0.06	

TABLE VI. Fit parameters obtained using the expansion of Eq. (3) rather than the Legendre expansion, shown for the present data in comparison with those obtained from a fit to the data of the Kharkov group reported by Gurev.¹⁵

Coefficient	Arkato v <i>et al.</i> 60 MeV	Present results 63-71 MeV	Arkato v <i>et al.</i> 80 MeV
A	24.88 ± 1.47	$18.90 \pm 1.25 \pm 1.00$	14.20 ± 1.67
β	0.99 ± 0.15	$1.48 \pm 0.15 \pm 0.10$	1.29 ± 0.23
γ	0.74 ± 0.30	$1.27 \pm 0.11 \pm 0.16$	1.58 ± 0.41
δ	0.02 ± 0.05	$0.07 \pm 0.07 \pm 0.05$	-0.08 ± 0.12
ϵ	-0.01 ± 0.30	$0.13 \pm 0.07 \pm 0.06$	-0.05 ± 0.08

augmented shell-model calculation of Gari and Hebach,⁵ and that of Casel and Sandhas,⁷ done within the framework of “exact” few-body theory. Both Gari and Hebach and Casel and Sandhas report a total cross section within the energy range of this experiment. The results of Gari and Hebach are shown in Fig. 11. Their independent-particle shell-model result, represented by the dotted curve, falls far below the data. The addition of nucleon correlations to the shell-model ground state of the ^4He nucleus results in the dot-dashed curve. The dashed curve represents the basic shell-model result with meson-exchange currents included. The solid curve is obtained when all three effects are included: shell-model one-body currents, modifications from nucleon correlations, and meson-exchange two-body currents. It is clear that the exchange current contribution is the dominant part of the cross section at these energies.

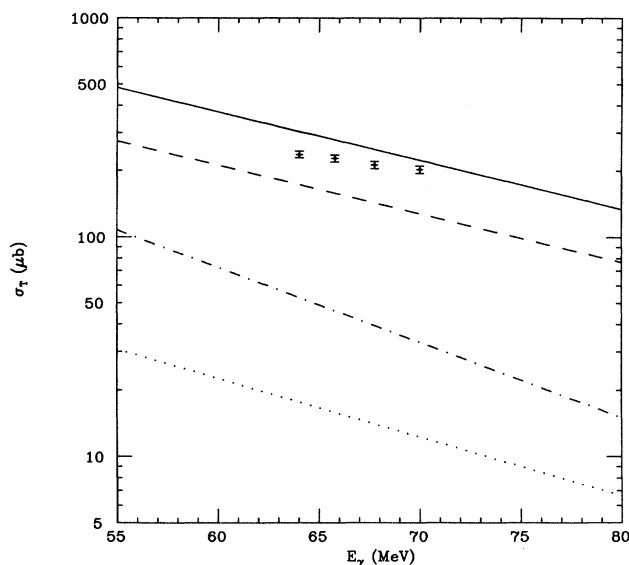


FIG. 11. Comparison of the present data with the total cross section calculated by Gari and Hebach. The dotted curve is their basic shell-model result, the dot-dashed curve includes shell-model plus nucleon correlation effects, the dashed curve is the shell-model plus exchange-current result, and the solid curve includes all three effects.

In their “exact” few-body calculations, Casel and Sandhas decompose the transition matrix element into what they call a Born term (in analogy to elastic two-body scattering) and a correction term that contains the final-state interactions. At energies above the giant dipole resonance, they report the Born result for the total cross section, saying that they expect effects from final-state interactions to be small. Their result is shown in Fig. 12. The fact that it is somewhat too small is not surprising, since they only included $E1$ transitions in the calculations.

Noguchi and Prats do not report a cross section in the energy range of this experiment, but they do plot the quantity β from Eq. (4), which is also called the asymmetry coefficient. Their value at 70 MeV for the $^4\text{He}(\gamma, p)^3\text{H}$ reaction is 0.86, less than the experimental value of 1.48 ± 0.25 . Gari and Hebach calculate the position of the maximum in the angular distribution, and report a value of 68° at 70 MeV. The experimental value is $62 \pm 3^\circ$.

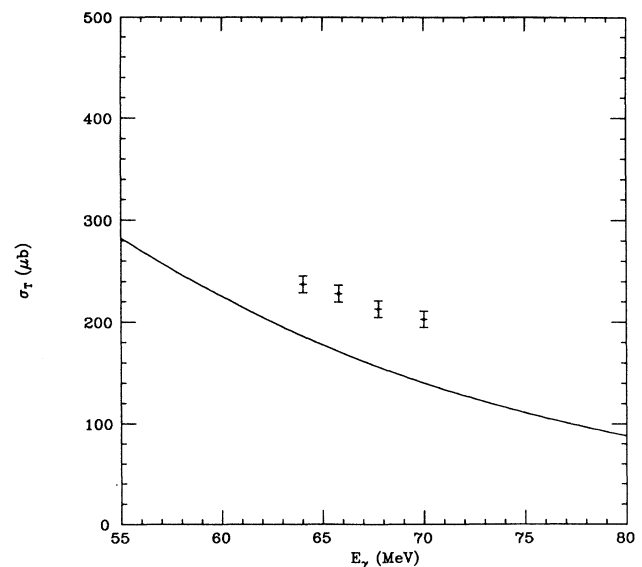


FIG. 12. Comparison of the present data with the total cross section calculated by Casel and Sandhas. The calculation contains their Born contribution only.

VI. SUMMARY AND CONCLUSIONS

The differential cross section for the reaction ${}^4\text{He}(\gamma, p){}^3\text{H}$ has been measured over the energy interval from 63 to 71 MeV for angles extending from 22° to 145° . The average statistical error on each data point representing an angular bin of 3° is less than 5%. An analysis of the systematic uncertainties inherent in the experiment and analysis procedure yielded an overall normalization error of 3%. The results are within 25% of several theoretical calculations. It is hoped that the new

data will prompt further refinements to these promising theoretical approaches.

ACKNOWLEDGMENTS

This work has been supported by the National Science Foundation under grants NSF-PHY85-20738, NSF-PHY86-10493, and NSF-PHY89-21146. We also wish to acknowledge the assistance of the Nuclear Physics Laboratory staff during the course of this work.

*Present address: CERN, CH-1211 Geneva 23, Switzerland.

¹Present address: Kelvin Laboratory, University of Glasgow, NEL, East Kilbride, G75 0QU, Scotland.

¹J. T. Londergan and C. M. Shakin, *Phys. Rev. Lett.* **28**, 1729 (1972).

²A. H. Chung, R. G. Johnson, and T. W. Donnelly, *Nucl. Phys.* **A235**, 1 (1974).

³D. Halderson and R. J. Philpott, *Phys. Rev. Lett.* **42**, 36 (1979).

⁴D. Halderson and R. J. Philpott, *Nucl. Phys.* **A359**, 365 (1981).

⁵M. Gari and H. Hebach, *Phys. Rep.* **72**, 1 (1981).

⁶A. J. F. Siegert, *Phys. Rev.* **52**, 787 (1937).

⁷A. Casel and W. Sandhas, *Czech. J. Phys.* **36**, 300 (1986).

⁸S. A. Sofianos (private communication).

⁹R. T. Jones, Ph.D. thesis, Virginia Polytechnic Institute and State University, 1988 (unpublished).

¹⁰D. S. Gemmel and G. A. Jones, *Nucl. Phys.* **33**, 102 (1962).

¹¹W. E. Meyerhof, M. Suffert, and W. Feldman, *Nucl. Phys.* **A148**, 211 (1970).

¹²A. M. Gorbunov, *Photonuclear and Photomesic Processes, Trudy*, edited by D. V. Skobel'tsyn (Consultants Bureau, New York, 1976), Vol. 71, p. 1.

¹³Yu. M. Arkatov, P. I. Vatsset, V. I. Voloshchuk, I. M. Prokhorets, A. F. Khodyachikh, and V. I. Chmil, *Yad. Fiz.* **16**, 12 (1972) [*Sov. J. Nucl. Phys.* **16**, 6 (1973)].

¹⁴Yu. M. Arkatov, P. I. Vatsset, V. I. Voloshchuk, V. N. Gur'ev, V. A. Zolenko, and I. M. Prokhorets, *Pis'ma Zh. Eksp. Teor. Fiz.* **28**, 710 (1978) [*JETP Lett.* **28**, 660 (1978)].

¹⁵The angular distributions from the Kharkov group can be found in V. N. Gur'ev, *Yad. Fiz.* **40**, 16 (1984) [*Sov. J. Nucl. Phys.* **40**, 10 (1984)]. This theoretical paper references a review article as the source of the experimental data: Fotodezintegratsiya legczaisich yader, P. I. Vatsset and V. I. Voloshchuk, in *Ocherki po istorii razvitiya yadernoi fiziki v SSSR* (Outline of the History of the Development of Nuclear Physics in the USSR), edited by E. V.

Inopin (Naukova dumka, Kiev, 1982), p. 221.

¹⁶Yu. M. Arkatov, P. I. Vatsset, V. I. Voloshchuk, V. N. Gur'ev, and A. F. Khodjachikh, *Ukr. Fiz. Ah.* **23**, 1818 (1978), in Russian.

¹⁷R. Bernabei, A. Chisholm, S. d'Angelo, M. P. De Pascale, P. Picozza, C. Schaerf, P. Belli, L. Casano, A. Incicchitti, D. Prospero, and B. Girolami, *Phys. Rev. Lett.* **57**, 1542 (1986).

¹⁸J. Knott, Ph.D. thesis, University of Illinois at Urbana-Champaign, 1988 (unpublished).

¹⁹P. D. Harty, R. T. Jones, J. E. Knott, P. T. Debevec, and D. A. Jenkins, *Nucl. Instrum. Methods* **A297**, 415 (1991).

²⁰C. T. Noguchi and F. Prats, *Phys. Rev. C* **14**, 1133 (1976).

²¹R. T. Jones, *Fifth Conference on Real-Time Computer Applications in Nuclear, Particle, and Plasma Physics* [IEEE Trans. Nucl. Sci. **NS34-4**, 917 (1987)].

²²V. White, P. Heinicke, E. Berman, P. Constanta-Fanourakis, B. MacKinnon, C. Moore, T. Nicinski, D. Petravic, R. Pordes, and L. Quigg, *Fifth Conference on Real-Time Computer Applications in Nuclear, Particle, and Plasma Physics* [IEEE Trans. Nucl. Sci. **NS34-4**, 763 (1987)].

²³B. Maréchal and M. Silva da Costa, *Nucl. Instrum. Methods* **A243**, 148 (1986).

²⁴R. Brun, F. Bruyant, M. Maire, A. C. McPherson, and P. Zanarini, *GEANT3 User's Guide*, CERN report CERN-DD/EE/84-1, 1986.

²⁵J. M. Cameron, *Can. J. Phys.* **62**, 1019 (1984).

²⁶The general form of the angular distribution is discussed by J. D. Irish, R. G. Johnson, B. L. Berman, B. J. Thomas, K. G. McNeill, and J. W. Jury, *Can. J. Phys.* **53**, 802 (1975). The discussion of this approximation is given by E. A. Vinokurov, V. I. Voloshchuk, V. B. Ganenko, E. S. Gorbenko, V. N. Gur'ev, V. A. Gushchin, V. P. Ermak, V. A. Zolenko, Yu. V. Zhebrovskii, I. Ya. Kolesnikov, Yu. P. Lyakhno, V. A. Nikitin, A. L. Rubashkin, and P. V. Sorokin, *Yad. Fiz.* **49**, 1233 (1989) [*Sov. J. Nucl. Phys.* **49**, 767 (1989)].